

Influence of alkalization over MIL-100(Fe) for enhanced VOCs adsorbents

Xinyu Xie

University of Shanghai for Science and Technology

Joy Thomas

National Taiwan University

Chang-Tang Chang

National I-Lan University

Hong Tao (✉ taohong@usst.edu.cn)

University of Shanghai for Science and Technology <https://orcid.org/0000-0002-2279-9752>

Research

Keywords: MIL-100(Fe) composites, mineralizing agent, green synthesis, dynamic adsorption, VOCs removal

Posted Date: April 6th, 2021

DOI: <https://doi.org/10.21203/rs.3.rs-370747/v1>

License: © ⓘ This work is licensed under a Creative Commons Attribution 4.0 International License.

[Read Full License](#)

Influence of alkalization over MIL-100(Fe) for enhanced VOCs adsorbents

Xinyu Xie¹, Joy Thomas^{2,3}, Chang-Tang Chang³, Hong Tao^{1*}

¹School of Environment and Architecture, University of Shanghai for Science and Technology,

Shanghai 200093, China

²Department of Chemical Engineering, National Taiwan University, Taipei 10617, Taiwan

³Department of Environmental Engineering, National I-Lan University, I-Lan 26047, Taiwan

*Corresponding author: taohong@usst.edu.cn

Abstract

Substantial attempts have been undertaken for the improvement of the air quality over decades; and Volatile Organic Compounds (VOCs) from the chemical and textile industries are truly listed as severe issue to be controlled. To come up with modus operandi for this issue, a novel composite of metal organic frameworks (MOFs) MIL-100(Fe) with salient tuned features of natrite was designed by a green and facile method. Mineralized composite MIL-100(Fe) exhibited enhanced crystallinity than pure MIL-100(Fe) as well showcased a higher surface area of 1300 m²g⁻¹. Through dynamic acetone pressure swing adsorption setup, MIL-0.05Na revealed an enhanced acetone adsorption of 210 mg g⁻¹ at room temperature. Gas phase adsorption isotherms confirmed the mono layer adsorption behavior. The kinetics models evaluated that the external mass transfer was the rate limiting step for surface adsorption. The thermodynamic study manifested that the adsorption reaction was spontaneous and exothermic. The proposed mechanism of adsorption was the act of physisorption which enriched the adsorbents reusability. This research work provides a futuristic vista to design mineralized Fe-MOFs composites for an energy saving adsorbents for VOCs removal.

Keywords: MIL-100(Fe) composites, mineralizing agent, green synthesis, dynamic adsorption, VOCs removal

1. Introduction

Volatile Organic Compounds (VOCs) known as a series of harmful air pollutants with high vapor pressure could bring about huge threat to human health and environment owing to the poisonousness, irritation, mutagenesis, and carcinogenesis [1, 2]. Among VOCs, acetone is a common volatile air pollutant, which is widely applied in pharmacy, paint, plastics, clothing

materials and chemical industries [3]. According to ACGIH (American Conference of Governmental Industrial Hygienists), the threshold limit value for acetone was set at 1000 ppm and the prolonged contact is poisonous to human health [4, 5]. Several methods have been employed to reduce the concentration of acetone such as adsorption, condensation, incineration, catalytic oxidation, etc [6]. Among these technologies, adsorption is considered as an effective and environment-friendly technique to control acetone emissions [7]. Especially, for industry concentration level, adsorption method has the advantages of simple operation, high adsorption efficiency, great design flexibility, low cost, etc [8-10]. It is important to look into for promising adsorbent with high performance and green process to adsorb acetone efficiently and reduce environment toxicity simultaneously.

Recently, metal organic frameworks (MOFs) have been fascinating owing to their huge specific surface area, well-defined crystalline structure, high porosities and controllable pore size [11]. MOFs are self-assembled by metal ions with organic ligands which possess a combined effect of organic-inorganic properties [12]. Due to the distinctive characteristics, MOFs have already been utilized in numerous fields including gas storage, sensors, adsorption, catalysis, etc [13, 14]. However, the synthetic methods of MOFs generally contain addition of harmful organic solvent such as methanol, N,N-dimethylformamide (DMF) and dichloromethane which can cause severe environmental pollution and health problem [15, 16]. With a view to the environment-friendly target, green process should be considered when developing MOFs for acetone removal.

MIL-100(Fe) is an iron-based MOFs which is composed of three-dimensional μ_3 -oxo-centered trimers of Fe octahedral and 1,3,5-benzenetricarboxylates (H_3BTC) anions [17]. As a typical mesoporous material, MIL-100(Fe) contains cages of 25 Å and 29 Å in diameter.

MIL-100(Fe) synthesized via hydrothermal route minimizes the utilization of organic solvent efficiently. Zhang et al. [18] synthesized MIL-100(Fe) with ethane-diamine to remove Pb(II) ions from water at 60 mg L⁻¹. Wang et al. [19] prepared Al@Fe-MOF to improve the adsorption performance (75 mg g⁻¹) for selenite. The ability for acetone removal is still a subject that hasn't been investigated. In addition, according to the in vivo toxicity assays, MIL-100(Fe) belongs to non-toxic materials [8]. Due to its sufficient porosity, good adsorption capacity and non-toxicity [18, 19], MIL-100(Fe) could be a promising green candidate for acetone removal. Nevertheless, the highly corrosive hydrofluoric acid (HF) was used frequently as mineralizing agent to promote the crystal growth of MIL-100(Fe) in the synthetic process [20]. Thus, it is necessary to search for fungible mineralizer with nontoxicity, low cost and ease of use, which can enhanced the adsorption ability of the adsorbent.

Na₂CO₃ has gradually been used as mineralization agents in preparing nanomaterials in recent years. Na₂CO₃ is a kind of inorganic salt with low basicity and nontoxicity, which could act as a promising green mineralizer [21]. Sreedhar et al. [22] prepared a ternary semiconducting oxide material with the addition of Na₂CO₃ as a mineralizer and the studies revealed that Na₂CO₃ could be conducive to the synthesis of the zinc tin oxide with high band gap. Fang et al [23] tested the adsorption capacity of MIL-100(Fe) mineralized by Na₂CO₃, tetramethyl ammonium hydroxide and HF towards Cr(VI) and found that Na₂CO₃ revealed better adsorption capacity (45 mg g⁻¹) than the samples without mineralizer. It is noteworthy to state that Fe-MOF composites are unprecedented approach for the adsorption of aliphatic ketones. The objectives of this research work are: 1) to inquire the characteristics of MIL-100(Fe) with Na₂CO₃ synthesized for different stoichiometry and 2) to assess the potential of utilizing MIL-100(Fe) as acetone

adsorbent.

2. Experimental

2.1. Chemicals and reagents

Ferric chloride (FeCl_3 , extra pure reagent, Ke-Hua Company), benzene-1,3,5-tricarboxylic acid (H_3BTC , extra pure reagent, Ke-Hua Company) and Sodium carbonate (Na_2CO_3 , extra pure reagent, Japan Reagent) were used to fabricate MIL-100(Fe) complexes. Acetone gas cylinder (Mix with N_2 gas with a concentration of 6000 ppm) was bought from a local gas seller (Jinde company) in Yilan county, Taiwan.

2.2. Synthesis of MIL-100(Fe) complexes

FeCl_3 (15 mM) and H_3BTC (10 mM) were dissolved in different concentration of 80 mL Na_2CO_3 solution (0, 0.01, 0.05 and 0.10 mM), sonicated for 0.5 h, put into an autoclave at 150 °C for 12 h. The synthesized sample was cooled to room temperature, purified by washing with Milli-Q (Lotun tech, Taiwan) by hot water and ethanol and then centrifuged. Then, the sample was kept at 100 °C for 10 h. Final product was mentioned as MIL-XNa, which 'X' means the concentration of Na_2CO_3 solution.

2.3. Characterization

Powder X-ray diffraction (XRD) results were attained under the radiation of $\text{Cu-K}\alpha$. The operation state was 40 mA and 40 kV with a scanning range between 5° to 80° at a scanning speed of 5° min^{-1} (Bruker D8 Advance diffract meter). N_2 sorption-desorption data were gained at -196 °C (Micromeritics ASAP 2020). Surface area, pore volume and pore size were calculated by Brunauer-Emmett-Teller (BET), Barrett-Joyner-Halenda (BJH), t-plot and density functional

theory (DFT) methods. The FT-IR spectra were obtained from SPECTRUM 100 instrument in the range of 650-2500 cm^{-1} . A simultaneous thermal analyzer (STA8000) was used to measure thermogravimetric properties from 30 to 800 $^{\circ}\text{C}$ on alumina sample pan with a heating rate of 10 $^{\circ}\text{C min}^{-1}$. Scanning Electron Microscope (SEM) was performed to study the morphology and granular size of the adsorbents (VEGA3 SBH).

2.4. Acetone Adsorption experiments

The acetone dynamic adsorption experimental setup is shown in Figure S1. All samples were pretreated at 373 K overnight to remove moisture and impurities before the acetone adsorption test. 0.5 g sample was added into a quartz tube of 700 mm in length and 10 mm in diameter. The N_2 and pure acetone cylinders were used to obtain the required gas mixture in the mixing chamber. The flow rate was controlled by rotameters connected with the mass flow controller (MFC, 5850E) to gain relatively stable concentration. The mixed acetone gas flows through the tube at an outflow of 600 mL min^{-1} . The adsorption isotherms data were tested for different temperature (298, 308, 318 and 328 K). The temperature was controlled by a tube furnace (HeYu company, 1000W). Gas Chromatography (GC, Clarus 680) was used to investigate the residual concentration continuously to get the breakthrough curves. The adsorption capacity could be obtained by the Eqs. (1):

$$q = C_0 \times (t \times 1 - A) / m \times Q \times 10^{-6} \quad (1)$$

Where C_0 is the original acetone concentration (mg m^{-3}); q represents the adsorption capacity of the material (mg g^{-1}); t is the adsorption saturation time (min); A is the integral area of the breakthrough curve; m is the quantity of the material (g) and Q is the total acetone outflow of 600

mL min⁻¹.

3. Results and Discussion

3.1. Physiochemical studies of adsorbents

The XRD patterns (Figure 1) of all samples demonstrated that the diffraction peaks were well matched with the results reported previously, expressed that MIL-100(Fe) and MIL-XNa were successfully synthesized [18]. With the adding of Na₂CO₃ as mineralizing agent, no impurity peaks appeared in the crystal system. The characteristic peaks of MIL-XNa observed at 10.7° and 11.1° were sharper and intense than that of pure MIL-100(Fe), which meant the crystallinity of MIL-XNa were improved with the increase of Na₂CO₃ in mineralization. The enhanced solubility and deprotonation of H₃BTC in alkaline Na₂CO₃ aqueous solution facilitated Fe³⁺ to combine with carboxylate more easily in the further crystallization of MIL-100(Fe) [23]. The reduction of unreacted H₃BTC provided homogeneous hydrothermal condition and enhanced the crystallization [24].

In the FTIR spectra (Figure 2), the adsorption peaks of MIL-XNa resembled to that of MIL-100(Fe). The peaks at 1701 cm⁻¹ belonged to the C=O stretching vibration of the carboxylates [25]. The peaks at 1628 and 1572 cm⁻¹ corresponded to the asymmetric stretching of the carboxylate, while the peaks at 1452 and 1383 cm⁻¹ could be assigned to the symmetric stretching of the carboxylates [11]. The peaks observed at 1111 and 943 cm⁻¹ were indication of C-H in-plane bending vibration of benzene. The peaks observed at 762 and 710 cm⁻¹ were expressions of C-H out-of-plane bending vibration of benzene [18]. The C-O stretching band at 1043 cm⁻¹ in MIL-100(Fe) indicated that monodentate coordination happened between Fe³⁺ and O atom of the carboxylates [19]. The disappeared C-O band in MIL-XNa samples exhibited that Fe³⁺ and O

atoms formed more bridged complexes instead of monodentate ones, suggesting that MIL-XNa performed more complete structure than MIL-100(Fe). MIL-0.05Na-AF was named for the MIL-0.05Na adsorbents after acetone adsorption. According to the literature, the intense C=O stretching band of acetone in the gas phase can be observed at 1740 cm^{-1} [26]. The C=O adsorption band of MIL-0.05Na-AF shifted to 1706 cm^{-1} , which can be ascribed to the adsorption of acetone on the material.

N_2 adsorption-desorption isotherms of all the materials is shown in Figure 3. The detailed pore structure parameters were presented in Table 1. In Figure 3a, steep rise could be observed at low pressure ($P/P_0 < 0.01$) and the isotherms of adsorbents exhibited type IV isotherm, which revealed the presence of micropores and mesopores [11]. MIL-100(Fe) exhibited H3 hysteresis loop, characteristic of the presence of slit-shaped pores [27]. However, MIL-XNa expressed obvious H1 hysteresis loop which suggested a high homogeneity of uniform and cylindrical pores [28]. In Figure 3b, distinct bimodal pores concentrated between 1.8 and 3.0 nm. The peaks shifted slightly to wider aperture range with intense rise of the mesoporous volume as the Na_2CO_3 increased. MIL-0.05Na denoted higher BET surface area ($1300\text{ m}^2\text{ g}^{-1}$) and larger pore volume ($0.779\text{ cm}^3\text{ g}^{-1}$) in comparing to other adsorbents. It suggested that Na_2CO_3 treatment not only retained the microstructure of MIL-100(Fe), but also restrained the unreacted protonated linker filling the mesopores, resulting in better textural properties [24].

The particle size of MIL-100(Fe) was approximately 200-300 nm, much larger than those of MIL-XNa samples around 100-200 nm (Figure 4). Aggregate of MIL-100(Fe) crystal could be observed in Figure 4a, which was compatible with the previous reports [23]. Apparently, all MIL-XNa samples (Figure 4b-d) performed less agglomeration, smaller particle size and better

crystallization than MIL-100(Fe). Amongst, MIL-0.05Na had the most uniform and dispersed crystal structure. However, too high concentration of Na_2CO_3 generated excess hydroxide anion, which inhibited the formation of the nucleus center and caused particles aggregation during the self-assembly process [8].

To understand the thermal stability, TGA and DTA of the samples were analyzed (Figure 5 and Figure S2). MIL-XNa maintained good stability and similar thermal properties compared with MIL-100(Fe). The weight loss had three stages, which was identified with the previous reports [8]. The first stage ranged from 30 °C to 320 °C, which was associated with the desorption of H_2O in the pores, the removal of crystal H_2O , the decomposition of sodium bicarbonate and the dihydroxylation of the iron clusters. The second region ranged from 320 °C to 500 °C, which was ascribed to the collapse of the BTC. The distinct positive peaks appeared at about 320 °C (Figure S2), indicating the decomposition of BTC was exothermal reaction. It was also observed that the final mass loss kept stable at 500 °C. MIL-0.05Na lost 37.7 % and 42.1 % of its initial weight in the first and second section, while MIL-100(Fe) lost 26.3 % and 49.2 %. The higher ratio of crystal water molecules was formed by the hydrolysis of Na_2CO_3 with H_3BTC , which caused less composition of residual carboxylic acids in MIL-XNa [23].

3.2. Adsorption studies over acetone

MIL-XNa exhibited larger acetone adsorption capacity than MIL-100(Fe) (Figure 6). Interestingly, MIL-0.05Na performed the longest breakthrough time for 70 min and adsorption saturation time for 390 min than other adsorbents. At 298 K, the acetone adsorption capacity of MIL-0.05Na was 173 mg g^{-1} and that of MIL-100(Fe) was 132 mg g^{-1} . The increase of former was up to 31.1% than the latter. In the hydrothermal process of MIL-100(Fe), there were a portion of

H₃BTC remained inside the pores of the adsorbent causing the iron metal sites poisoned and finally lost part of the holes [8]. The hydrolysis of Na₂CO₃ brought in hydroxyl, facilitating the dissolution of protonated carboxylic acids (Scheme 1). The BTC ligand with enhanced solubility in the synthesis inhibited the pores filling and concurrently increased the amount of mesopores in MIL-0.05Na [24]. The synergistic effect of hierarchical pores with molecular accessibility and abundant adsorption sites further provided the enhanced acetone adsorption capacity [29].

3.3. Extrinsic factors impacting adsorption

In Figure S3, the breakthrough experiment was tested at different concentration (400, 600, 800, 1000 ppm) at 298K. With the higher concentration, the breakthrough time became shorter and the adsorption capacity became higher. The maximum adsorption capacity of MIL-100(Fe) and MIL-0.05Na was up to 200 mg g⁻¹ and 210 mg g⁻¹ at 1000 ppm, respectively. The larger adsorption capacity at high concentration was due to the effect of concentration gradient, increasing the number of molecules that could be absorbed into the pore per unit time, making the adsorbents reach saturation faster [30].

Figure 7 pictured the temperature influence on acetone adsorption of MIL-0.05Na at 298, 308, 318 and 328 K with the initial acetone concentration of 400 ppm. Note that when the temperature rises, the adsorption capacity of MIL-0.05Na decreased distinctly, which denotes that physisorption happened between MIL-0.05Na and acetone [15]. The adsorption capacity of MIL-0.05Na at 298 K and at 328 K was 173 mg g⁻¹ and 60 mg g⁻¹, respectively. The increase of temperature resulted in the intensification of Brownian motion and the decrease of electrostatic interactions between molecules. The collision rate between acetone molecules and the adsorption materials accelerated, which led to the low adsorption capacity [31]. Table 2 listed that acetone

adsorption capacity of some other adsorbents such as various activated carbon and MOFs. Obviously, MIL-0.05Na has quite promising acetone adsorption capacity at relatively low inlet concentration, showcasing that MIL-0.05Na is a potential adsorbent to remove acetone.

3.4. Gas adsorption isotherms

To understand the mechanism between the adsorbate on adsorbent gas, Langmuir model, Freundlich model and Temkin model were selected as the fitting models for MIL-100(Fe) and MIL-0.05Na. The related equations were listed below in Eqs. (2), (3) and (4) [32]:

$$Q = C_0 ab / (1 + aC_0) \quad (2)$$

$$Q = KC_0^{1/n} \quad (3)$$

$$Q = B(\ln K_T + \ln C_0) \quad (4)$$

Where Q is the adsorption amount at equilibrium concentration (mg g^{-1}); C_0 is the initial acetone concentration (mg m^{-3}); a is Langmuir adsorption constant; b is the saturated adsorption capacity (mg g^{-1}); K and n are Freundlich adsorption constant; B is Temkin adsorption constant and K_T is equilibrium binding energy constant.

Figure 8 and Table S1 plotted the fitting parameters and correlation coefficients. The well Langmuir fitting data of MIL-100(Fe) and MIL-0.05Na for acetone indicated that the acetone adsorption was a physical monomolecular-layer and homogeneous adsorption [33]. According to the Eqs. (2), the saturated adsorption capacity of MIL-100(Fe) and MIL-0.05Na were 249 and 311 mg g^{-1} , respectively [34]. The result of Freundlich and Temkin model are presented in Figure S4.

3.5. Gas adsorption kinetics

Pseudo-first-order (PFO) and pseudo-second-order (PSO) kinetic model were used to study the result at 298 K for different inlet concentrations (400, 600, 800 and 1000 ppm) to realize the kinetic behaviours (Figure 9). The PFO and PSO model were listed below in Eqs. (5), (6) and (7) [29, 34].

$$q_t = q_e / (1 - e^{-k_1 t}) \quad (5)$$

$$\log(q_e - q_t) = \log q_e - k_1 t / 2.303 \quad (6)$$

$$t/q_t = 1/k_2 q_e^2 + t/q_e \quad (7)$$

Where q_e (mg g^{-1}) is the adsorption amount at equilibrium adsorption, q_t (mg g^{-1}) is the adsorption amount at reaction time t (min); k_1 (min^{-1}) and k_2 ($\text{g mg}^{-1} \text{min}^{-1}$) are the PFO and PSO kinetic reaction rate constants, respectively.

As shown in Table S2, the PFO model fitted better for MIL-100(Fe) and MIL-0.05Na. It exhibited that the surface adsorption process was mostly commanded by external mass transfer. When initial acetone concentration increased, the reaction rate rised accordingly contributing the enhancement of external mass transfer.

3.6. Analysis of intra-particle diffusion model

To study the intra-particle diffusion process, Weber and Morris model was applied. The intra-particle diffusion equation is described as follow in Eqs. (8) [35].

$$q_t = k_{id} t^{1/2} + C \quad (8)$$

Where q_t (mg g^{-1}) is the adsorbed amount at reaction time t (min); k_{id} ($\text{mg g}^{-1} \text{min}^{-1/2}$) is the intra-particle diffusion rate constant; C is a boundary layer thickness constant.

In Figure 10, plots of q_t versus $t^{1/2}$ claimed multi-linearity characterizations and all the fitting curves did not go through the origin. It demonstrated that the adsorption process of MIL-100(Fe) and MIL-0.05Na were jointly mastered by intra-particle diffusion and other steps. In first stage, the adsorption happened rapidly on external surface of the adsorbent. In next stage, the adsorbate filled into the pore inside the materials going into the gradual adsorption process, where intra-particle diffusion was rate-controlled [35]. Furthermore, the rate parameters were obtained from the slope of the plot, emphasizing that the intraparticle diffusion rate of MIL-0.05Na was much higher, which was more conducive to the adsorption of acetone [37].

3.7. Thermodynamic behavioral studies

From the temperature experiment results, the adsorption process could be assumed as an exothermic reaction. In order to study the thermodynamic characteristics, the Gibbs free energy change (ΔG) was obtained according to the Eqs. (9) [33].

$$\Delta G = -RT \ln K_L \quad (9)$$

Where K_L refers to the Langmuir adsorption constant (L mol^{-1}), which can be calculated from the Langmuir adsorption isotherm.

The enthalpy change (ΔH) and entropy change (ΔS) can be achieved from the slope and intercept of the Eqs. (10), respectively [33].

$$\Delta G = \Delta H - T\Delta S \quad (10)$$

The fitting results were shown in Figure S5 and Table S3. It indicated that the acetone

adsorption on MIL-0.05Na was spontaneous when ΔG was negative. It conveyed that the reaction was exothermic when ΔH was negative. The adsorption was an entropy increment and non-order process when ΔS were positive.

3.8. Recycling experiment

The recycling performance of MIL-0.05Na was investigated at 298 K with the initial acetone concentration of 800 ppm for 3 times. After adsorption saturation, the adsorbent was revival mode for 12 h at 423 K. In Figure S6, the adsorption efficiency reached 95, 91 and 88%, respectively, from first to third cycle, showing relative stable adsorption capacity and reproducibility. It was illustrated that the adsorbent had some holes, which could not be reversibly desorbed with physical method. The reason might be that the high temperature caused damage to the structure and resulted in loss of adsorption sites gradually in the desorption process.

4. Conclusions

MIL-100(Fe) and a series of MIL-XNa were synthesized with a green and facile procedure with the Na_2CO_3 as mineralizer to enhance the adsorption of acetone. The characterizations confirmed that MIL-0.05Na extended the higher BET surface area of $1300 \text{ m}^2\text{g}^{-1}$ and pore volume of $0.779 \text{ cm}^3 \text{ g}^{-1}$. The particle size of MIL-0.05Na was much smaller and more uniform than other samples due to the enhanced deprotonation of carboxylic acids by Na_2CO_3 during the hydrothermal process. MIL-0.05Na claimed the enhanced acetone adsorption capacity of 210 mg g^{-1} . The adsorption isotherm results and thermodynamic data manifested that the acetone adsorption on MIL-0.05Na was a physical spontaneous entropy incremental process. The kinetic and intra-particle diffusion analysis revealed the surface adsorption process was jointly controlled by

external mass transfer and intraparticle diffusion. The properties of nontoxicity, eco-friendly and higher adsorption tendency towards acetone made the MIL-0.05Na promising green MOFs for the VOCs adsorption.

Declarations

Availability of data and materials

All data generated or analyzed during this study are examined by our group and certified for several times.

Competing interests

The authors declare they have no competing interests.

Funding

This work was sponsored financially by the Natural Science Foundation of China (No.51679140).

Authors' contributions

Xinyu Xie provided real test data and wrote the paper, Joy Thomas reviewed and edited the paper,

Chang-Tang Chang analyzed the test data, and Hong Tao organized the researched full structure.

All authors read and approved the final manuscript.

Acknowledgments

The authors wish to thank for the finance by Natural Science Foundation of China (No.51679140) and the School of Environment and Architecture, University of Shanghai for Science and Technology, China for support of research at the university.

Authors' information (optional)

1. Xinyu Xie: School of Environment and Architecture, University of Shanghai for Science and Technology, Shanghai 200093, China.
2. Joy Thomas: Department of Chemical Engineering, National Taiwan University, Teipei 10617, Taiwan; and Department of Environmental Engineering, National I-Lan University, I-Lan 26047, Taiwan.

3. Chang-Tang Chang: Department of Environmental Engineering, National I-Lan University,
I-Lan, 26047, Taiwan.
4. Hong Tao: School of Environment and Architecture, University of Shanghai for Science and
Technology, Shanghai 200093, China.

References

1. Mo Y, Li H, Zhou K, Ma X, Guo Y, Wang S, Li L. Acetone adsorption to (BeO) 12,(MgO) 12 and (ZnO) 12 nanoparticles and their graphene composites: A density functional theory (DFT) study. *Appl Surf Sci.* 2019;469:962-973.
2. Yang HH , Gupta SK , Dhital NB. Emission factor, relative ozone formation potential and relative carcinogenic risk assessment of VOCs emitted from manufacturing industries. *Sustain Environ Res.*2020;30:28-42.
3. Shrestha S, Baral B, Dhital NB, Yang HH. Assessing air pollution tolerance of plant species in vegetation traffic barriers in Kathmandu Valley, Nepal. *Sustain Environ Res.* 2021;31:3.
4. Lemraski MS And Nadimi E. Acetone gas sensing mechanism on zinc oxide surfaces: A first principles calculation. *Surf Sci.* 2017;657:96-103.
5. Simón D, Quaranta N, Gass S, Procaccini R, Cristóbal A. Ceramic bricks containing Ni ions from contaminated biomass used as an adsorbent. *Sustain Environ Res.* 2020;30:26.
6. Wang Y, Tao H, Yu D, Chang C. Performance assessment of ordered porous electrospun honeycomb fibers for the removal of atmospheric polar volatile organic compounds. *Nanomater.* 2018;8(5):350-364.
7. Choi WS, Hwang MJ, Kwon YJ, Jung SH, Youn Y, Balathanigaimani MS, Lee JW, Hwang KJ, Shim WG. Radio-Frequency Thermal Plasma Treated Activated Carbon Impregnated with Mn and Ag for Volatile Organic Compounds Adsorption. *J Nanosci Nanotech.* 2020;20(7):4423-4427.
8. Seo YK, Yoon JW, Lee JS, Lee UH, Hwang YK, Jun CH, Horcajada P, Serre C, Chang J S. Large scale fluorine-free synthesis of hierarchically porous iron (III) trimesate MIL-100 (Fe) with a zeolite MTN topology. *Micro Mesos Mater.* 2012;157:137-145.
9. Hamedi A, Zarandi MB, Nateghi MR. Highly efficient removal of dye pollutants by MIL-101 (Fe) metal-organic framework loaded magnetic particles mediated by Poly L-Dopa. *J Environ Chem Eng.* 2019;7(1):102882-102893.
10. Xie Q, Li Y, Lv Z, Zhou H, Yang X, Chen J, Guo H. Effective adsorption and removal of

- phosphate from aqueous solutions and eutrophic water by Fe-based MOFs of MIL-101. *Scientific Reports*, 2017;7(1):1-15.
11. Li S, Cui J, Wu X, Zhang X, Hu Q, Hou X. Rapid in situ microwave synthesis of Fe₃O₄@ MIL-100 (Fe) for aqueous diclofenac sodium removal through integrated adsorption and photodegradation. *J Hazard Mater.*, 2019;373:408-416.
 12. Ribeiro AM, Campo MC, Narin G, Santos JC, Ferreira A, Chang JS, Hwang YK, Seo YK, Loureiro JM, Rodrigues AE. Pressure swing adsorption process for the separation of nitrogen and propylene with a MOF adsorbent MIL-100 (Fe). *Sep Purif Tech.* 2013;110:101-111.
 13. Zan J, Song H, Zuo S, Chen X, Xia D, Li D. MIL-53 (Fe)-derived Fe₂O₃ with oxygen vacancy as Fenton-like photocatalysts for the elimination of toxic organics in wastewater. *J Cleaner Produc.* 2020;246:118971-118983.
 14. Seo YK, Chitale SK, Lee U, Patil P, Chang JS, Hwang YK. Formation of polyaniline-MOF nanocomposites using nano-sized Fe (III)-MOF for humidity sensing application. *J Nanosci Nanotech.* 2019;19(12):8157-8162.
 15. Zhou X, Huang W, Shi J, Zhao Z, Xia Q, Li Y, Wang H, Li Z. A novel MOF/graphene oxide composite GrO@ MIL-101 with high adsorption capacity for acetone. *J Mater Chem A*, 2014;2(13):4722-4730.
 16. Leng K, Sun Y, Li X, Sun S, Xu W. Rapid synthesis of metal-organic frameworks MIL-101 (Cr) without the addition of solvent and hydrofluoric acid. *Crystal Growth Desig.* 2016;16(3):1168-1171.
 17. Zhang X, Shi Q, Shen B, Hu Z, Zhang X. MIL-100 (Fe) supported Mn-based catalyst and its behavior in Hg⁰ removal from flue gas. *J Hazard Mater.* 2020;381:121003-121011.
 18. Zhang H, Wen J, Fang Y, Zhang S, Zeng G. Influence of fulvic acid on Pb (II) removal from water using a post-synthetically modified MIL-100 (Fe). *J Coll Inter Sci.* 2019;551:155-163.
 19. Wang R, Xu H, Zhang K, Wei S, Wu D. High-quality Al@ Fe-MOF prepared using Fe-MOF as a micro-reactor to improve adsorption performance for selenite. *J Hazard Mater.* 2019;364:272-280.
 20. Horcajada P, Surblé S, Serre C, Hong DY, Seo YK, Chang JS, Grenèche JM, Margiolaki I,

- Férey G. Synthesis and catalytic properties of MIL-100(Fe), an iron (III) carboxylate with large pores. *Chem Communi.* 2007;27:2820-2822.
21. Xiao Q, Zhong Y, Zhu W, Chen T, Wang, L. Synthesis of bimodal mesoporous molecular sieves under mild conditions with salts as mineralization agents. *Micro Meso Mater.* 2008;116:339-343.
 22. Reddy V, Vasudevarao V, Sreedhar D. Synthesis and Analysis of Ternary Oxide Nanomaterial for Electro-Thermal Applications. *2nd Interl Confer Nanomater Tech.* 2014;10:116-123.
 23. Fang Y, Wen J, Zeng G, Jia F, Zhang S, Peng Z, Zhang H. Effect of mineralizing agents on the adsorption performance of metal-organic framework MIL-100(Fe) towards chromium(VI). *Chem Eng J.* 2018;337:532-450.
 24. Manuel SS, Negash G, Kenya D, Manuel DG, Yonas C, Isabel D. Synthesis of metal-organic frameworks in water at room temperature: salts as linker sources. *Green Chem.* 2017;17:1500-1510.
 25. Zhang ZY, Liu X, Mao H, Wang C, Du X, Cheng H, Zhuang J. Effects of iron salts on synthesis of MIL-100(Fe) and photocatalytic activity. *J Mater Eng.* 2019;47:71-78.
 26. Terencio T, Renzo FD, Berthomieu D, Trens P. Adsorption of acetone vapor by Cu-BTC: An experimental and computational study. *J Phys Chem C*, 2013;117:26156-26165.
 27. Pawar R, Lalhmunsiana R, Ingole PG, Lee SM. Use of activated bentonite-alginate composite beads for efficient removal of toxic Cu^{2+} and Pb^{2+} ions from aquatic environment. *Inter J Biolo Macromol*, 2020;164:3145-3154.
 28. Svidrytski A, Hlushkou D, Thommes M, Monson PA, Tallarek U. Modeling the Impact of Mesoporous Silica Microstructures on the Adsorption Hysteresis Loop. *J Phys Chem C*, 2020;124:21646-21655.
 29. Yu X, Liu S, Lin G, Zhu X, Zhang S. Insight into the significant roles of microstructures and functional groups on carbonaceous surfaces for acetone adsorption. *RSC Advances*, 2018;8:21541-21550.
 30. Dawodu FA, Abonyi CJ, Akpomie KG. Feldspar banana peel composite adsorbent for efficient crude oil removal from solution. *Appl Water Sci.* 2021;11:3-13.
 31. SeeraS DK, Kundu D, Gami P, Naik PK, Banerje T. Synthesis and characterization of

- xylan-gelatin cross-linked reusable hydrogel for the adsorption of methylene blue. *Carbohydrate Polymers*, 2021;256:117520-117532.
32. Tsai JH, Chiang HM, Huang GY, Chiang HL. Adsorption characteristics of acetone, chloroform and acetonitrile on sludge-derived adsorbent, commercial granular activated carbon and activated carbon fibers. *J Hazard Mater*. 2018;154:1183-1191.
 33. Zhao Z, Li X, Li Z. Adsorption equilibrium and kinetics of p-xylene on chromium-based metal organic framework MIL-101. *Chem Eng J*. 2011;173:150-157.
 34. Yu X, Liu S, Lin G, Yang Y, Zhang S, Zhao H, Zheng C. KOH-activated hydrochar with engineered porosity as sustainable adsorbent for volatile organic compounds. *Coll Surf A*, 2020;588:124372-124380.
 35. Wu FC, Tseng RL, Juang RS. Initial behavior of intraparticle diffusion model used in the description of adsorption kinetics. *Chem Eng J*. 2009;153:1-8.
 36. Yang W, Cloete S, Morud J, Amini S. An Effective Reaction Rate Model for Gas-Solid Reactions with High Intra-Particle Diffusion Resistance. *Interl J Chem Reac Eng*. 2016;14:331-442.
 37. Trinh QH, Gandhi MS, Mok YS. Adsorption and plasma-catalytic oxidation of acetone over zeolite-supported silver catalyst. *J Appl Phys*. 2015;54:1-7.
 38. Chen R, Han N, Li L, Wang S, Ma X, Wang C, Li H, Zeng L. Fundamental understanding of oxygen content in activated carbon on acetone adsorption desorption. *Appl Surf Sci*. 2019;508:145211-145217.

Table 1 Surface dimensions of MIL-100(Fe) vs MIL-XNa

Samples	Total BET Surface Area (m ² g ⁻¹)	Microporous Surface Area (m ² g ⁻¹)	Mesoporous Surface Area (m ² g ⁻¹)	Total pore volume (cm ³ g ⁻¹)	Microporous volume (cm ³ g ⁻¹)	Mesoporous volume (cm ³ g ⁻¹)
MIL-100(Fe)	802	567	235	0.54	0.25	0.29
MIL-0.01Na	1079	485	625	0.66	0.21	0.45
MIL-0.05Na	1300	573	727	0.78	0.25	0.53
MIL-0.10Na	1236	534	702	0.68	0.23	0.45

Table 2 Performance of acetone capture on different adsorbents

Adsorbents	Q _{max} (mg g ⁻¹)	Inlet Concentration	Temperature (K)	References
MIL-100(Fe)	249	1000 ppm	298	This work
MIL-0.05Na	311	1000 ppm	298	This work
PC	226	1000 ppm	298	[34]
Ag-cated zeolite	62	1000 ppm	298	[37]
AC	70	400 ppm	293	[32]
PH	123	19.3 kPa	298	[38]

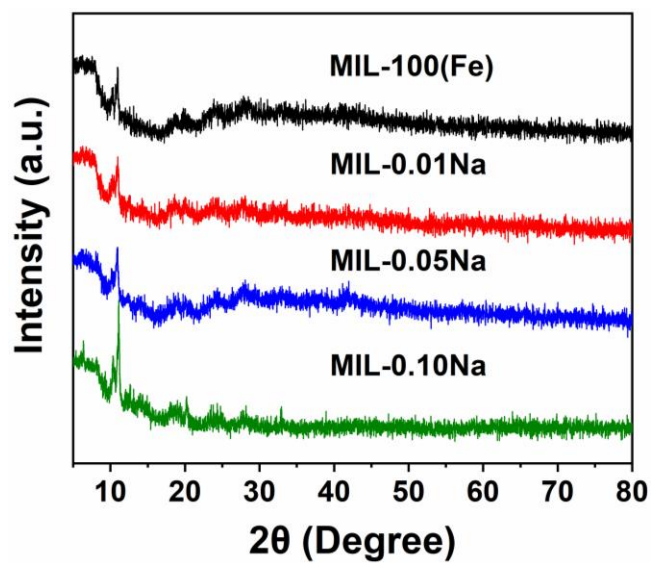


Figure 1. XRD patterns MIL-100(Fe) and MIL-XNa

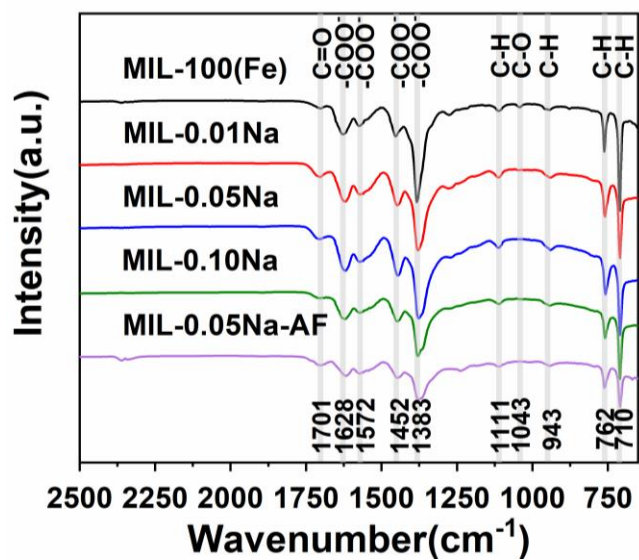


Figure 2. FTIR of MIL-100(Fe) and MIL-XNa

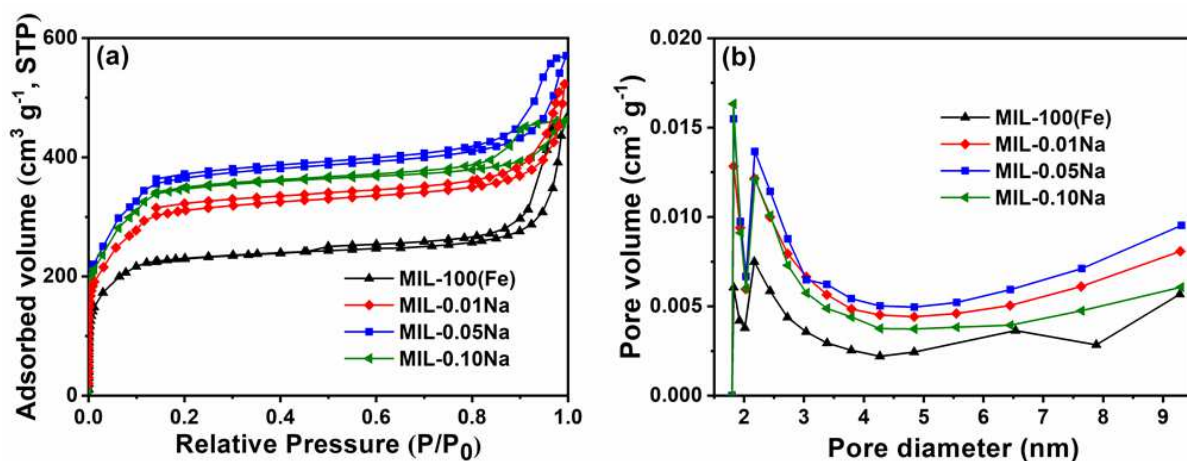


Figure 3. MIL-100(Fe) and MIL-XNa (a) N₂ adsorption-desorption isotherms and (b) pore size distribution

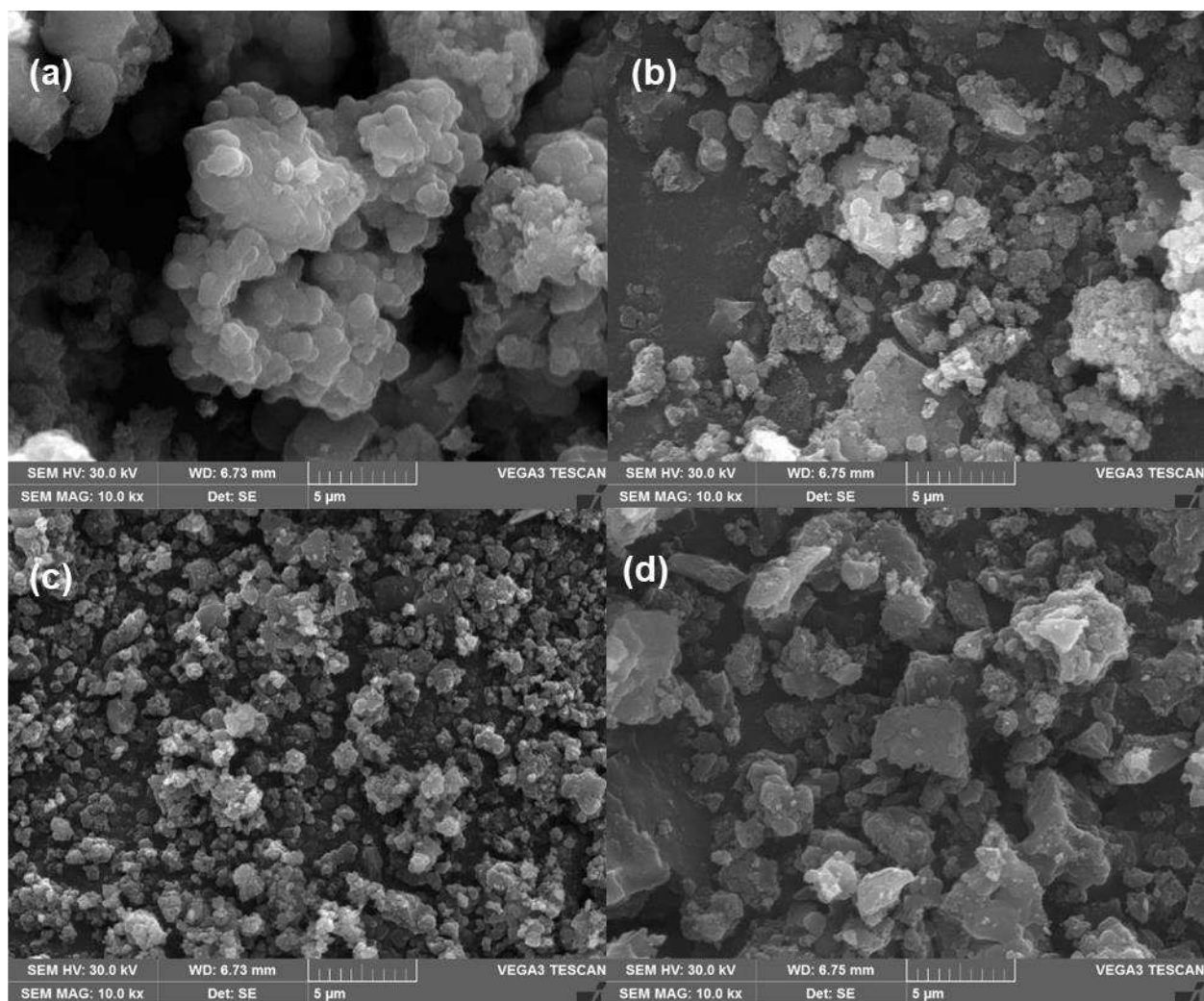


Figure 4. SEM of (a) MIL-100(Fe) (b) MIL-0.01Na (c) MIL-0.05Na and (d) MIL-0.10Na

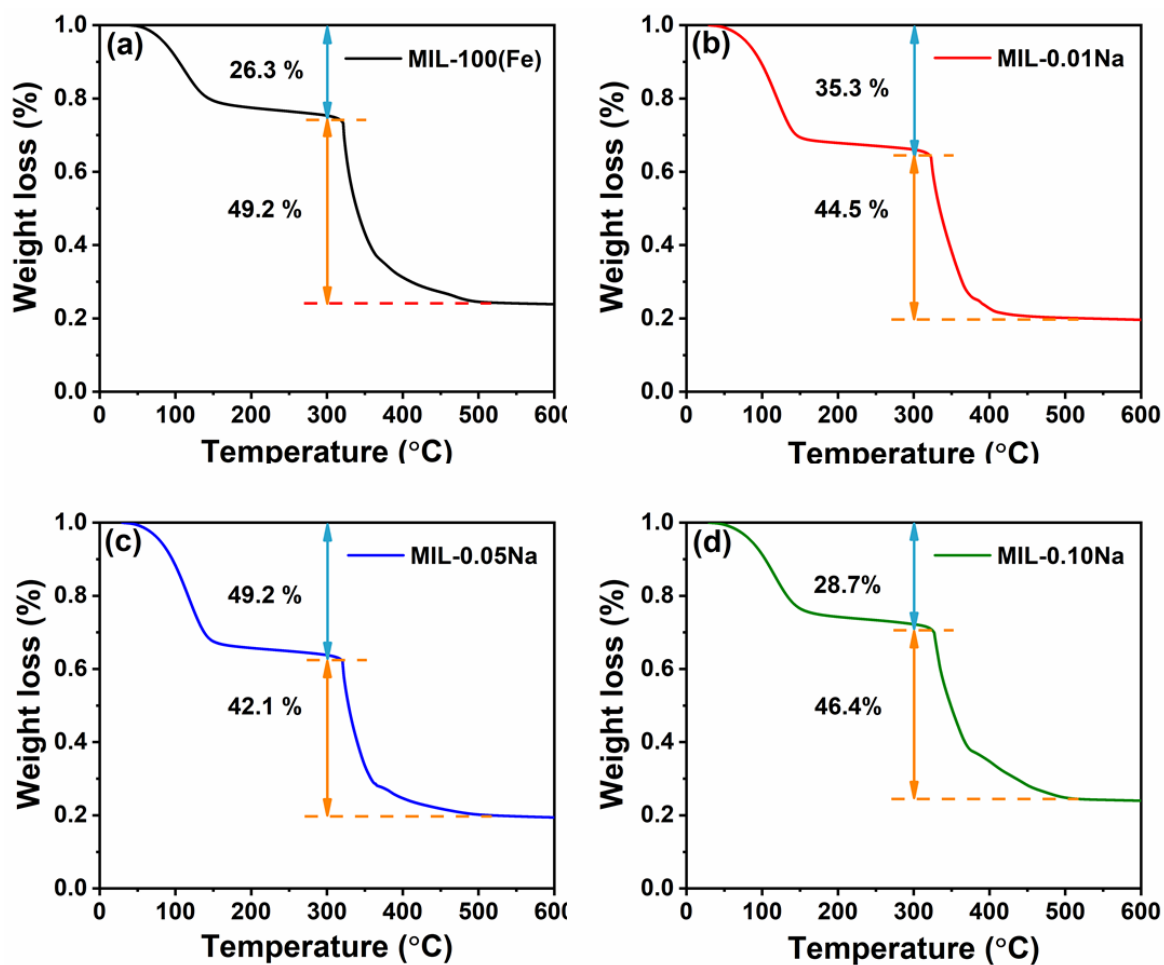


Figure 5. TGA of (a) MIL-100(Fe) (b) MIL-0.01Na (c) MIL-0.05Na and (d) MIL-0.10Na

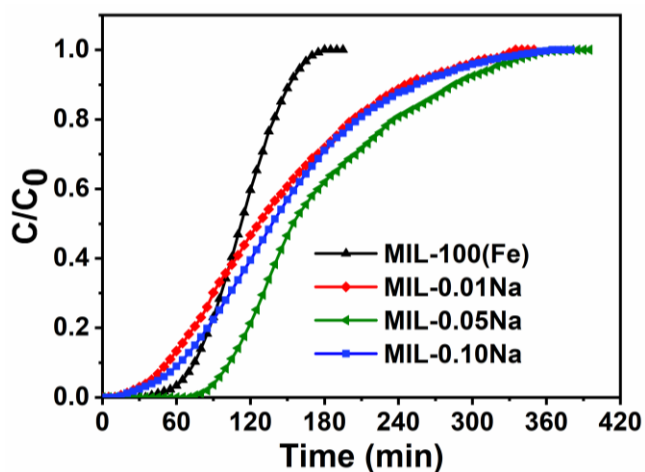


Figure 6. Breakthrough curves with MIL-100(Fe) and MIL-XNa at 400 ppm and 298 K

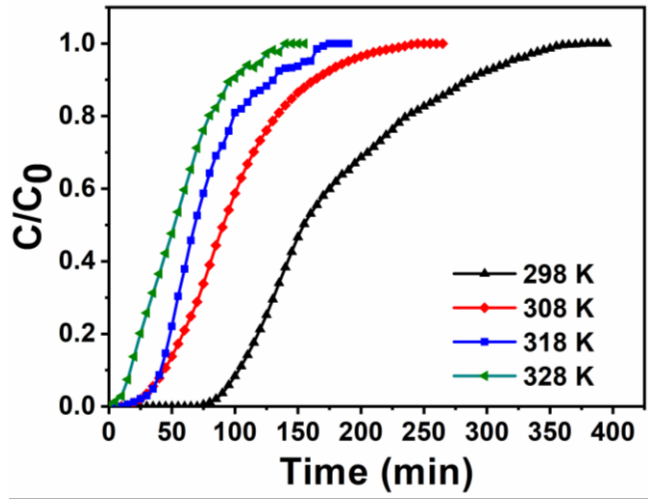


Figure 7. Breakthrough curves with MIL-0.05Na at different temperature

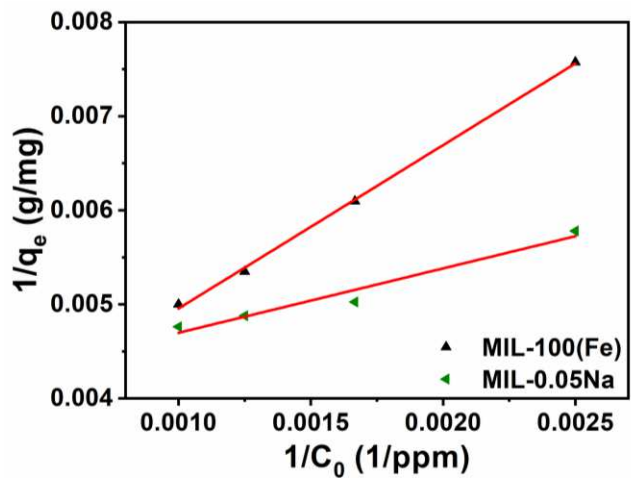


Figure 8. Adsorption isotherms: Langmuir model

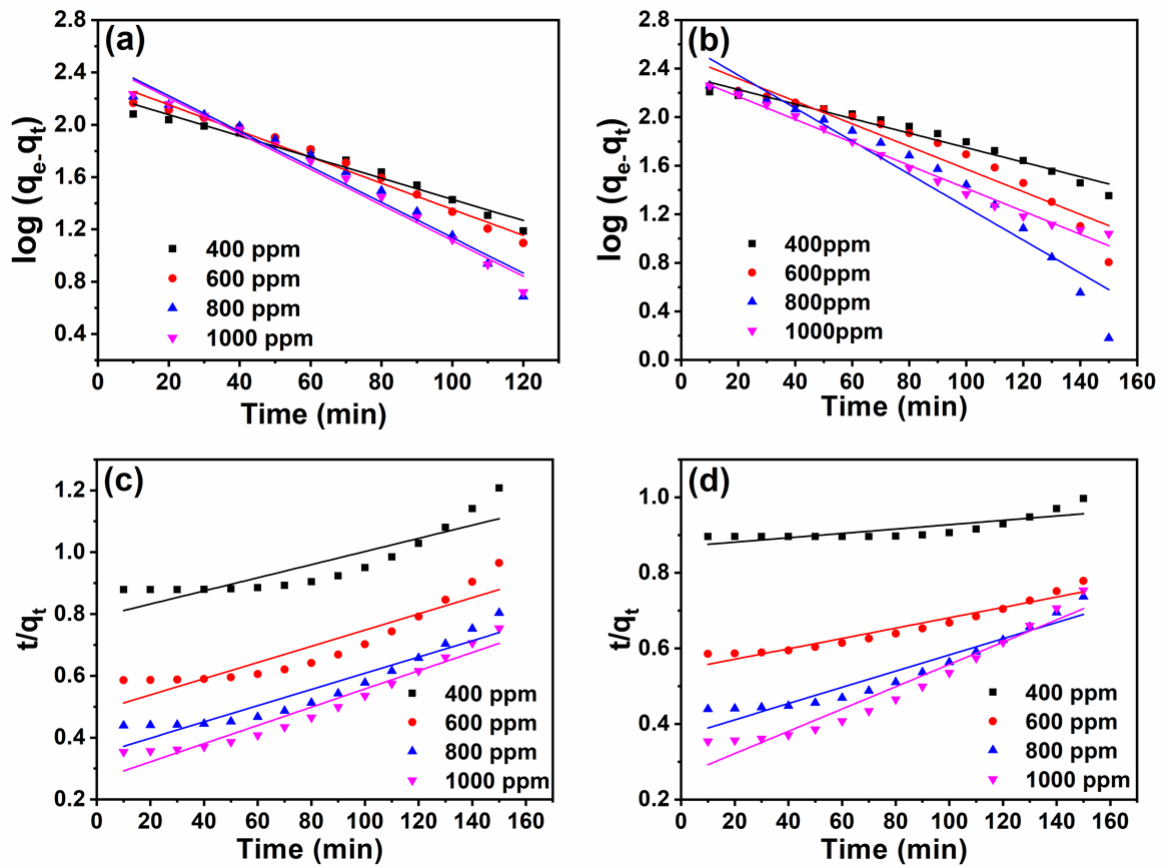


Figure 9. Kinetic fitting of (a) MIL-100(Fe) PFO model (b) MIL-100(Fe) PSO model (c) MIL-0.05Na PFO model and (d) MIL-0.05Na PSO model

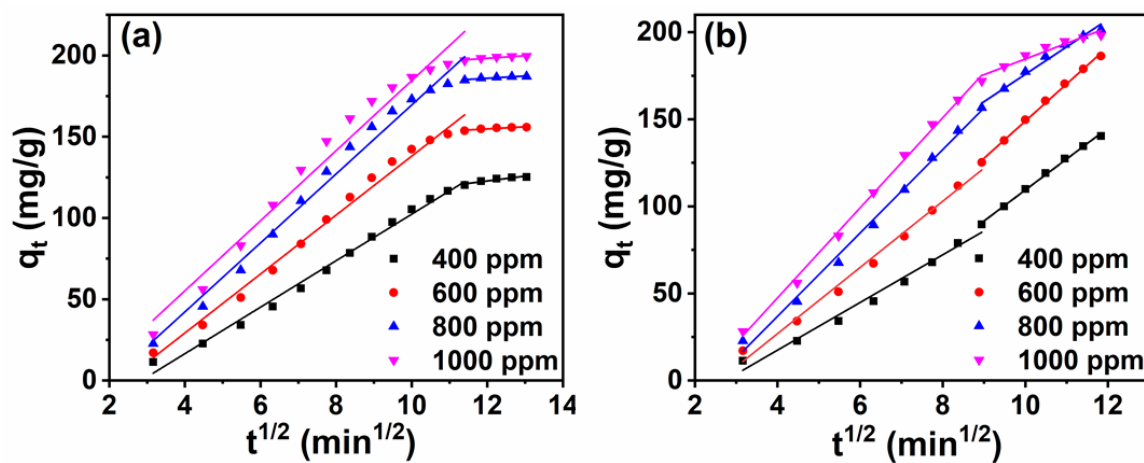
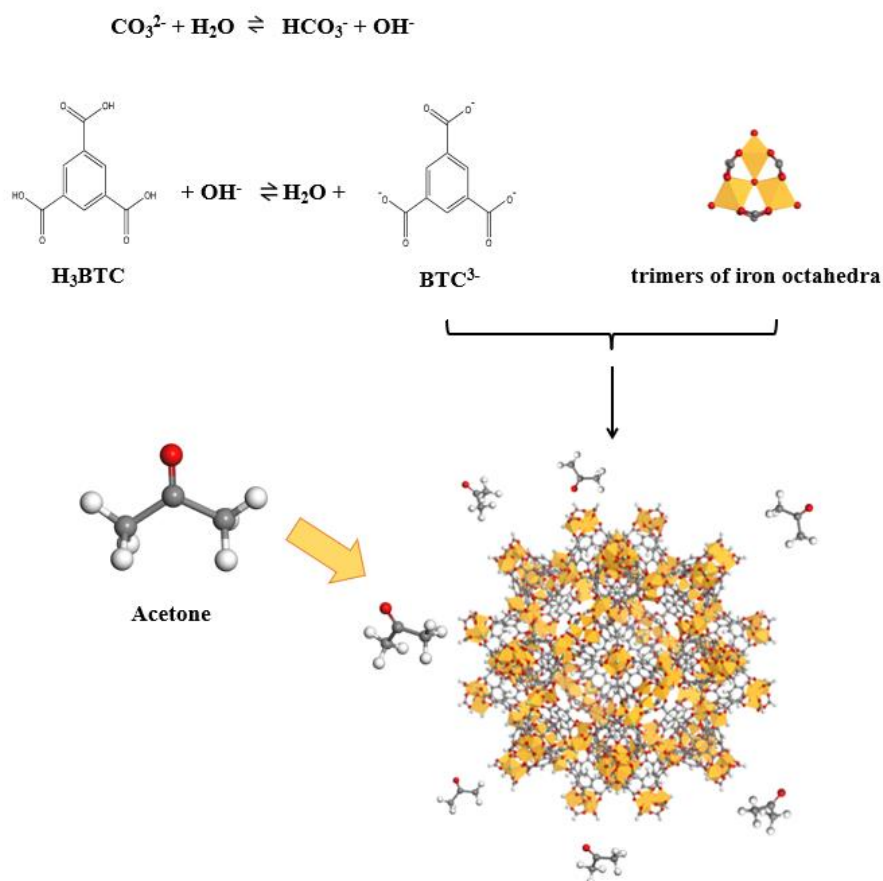


Figure 10. Kinetics of acetone adsorption with (a) MIL-100(Fe) and (b) MIL-0.05Na according to the intra-particle diffusion model



Scheme 1. Mechanism of acetone adsorption on MIL-100(Fe) mineralized by Na_2CO_3

Figures

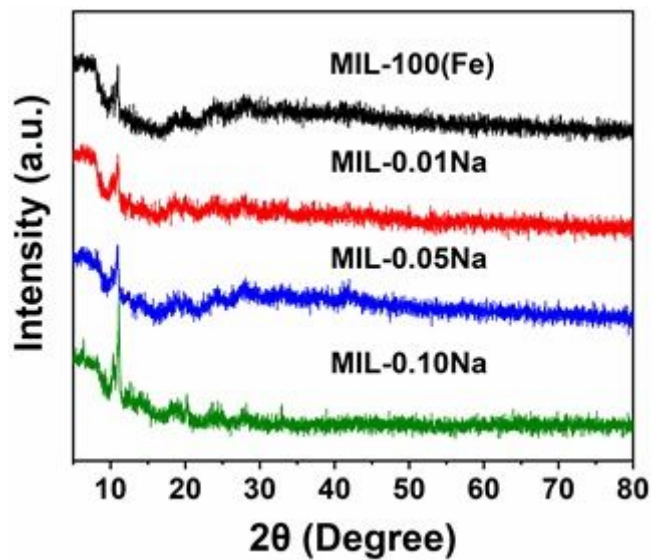


Figure 1

XRD patterns MIL-100(Fe) and MIL-XNa

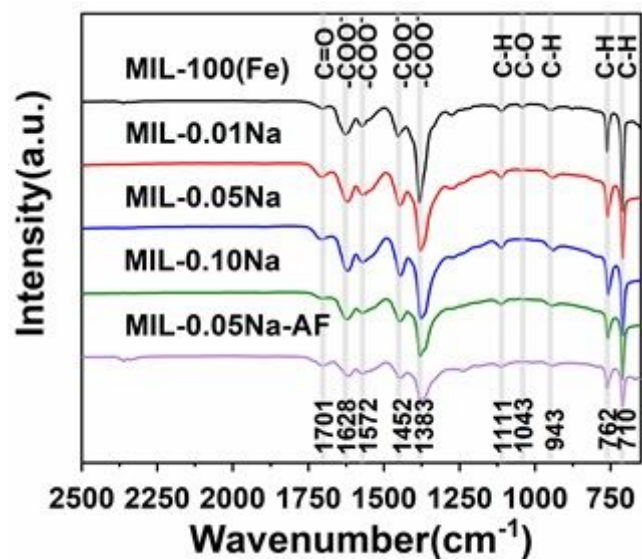


Figure 2

FTIR of MIL-100(Fe) and MIL-XNa

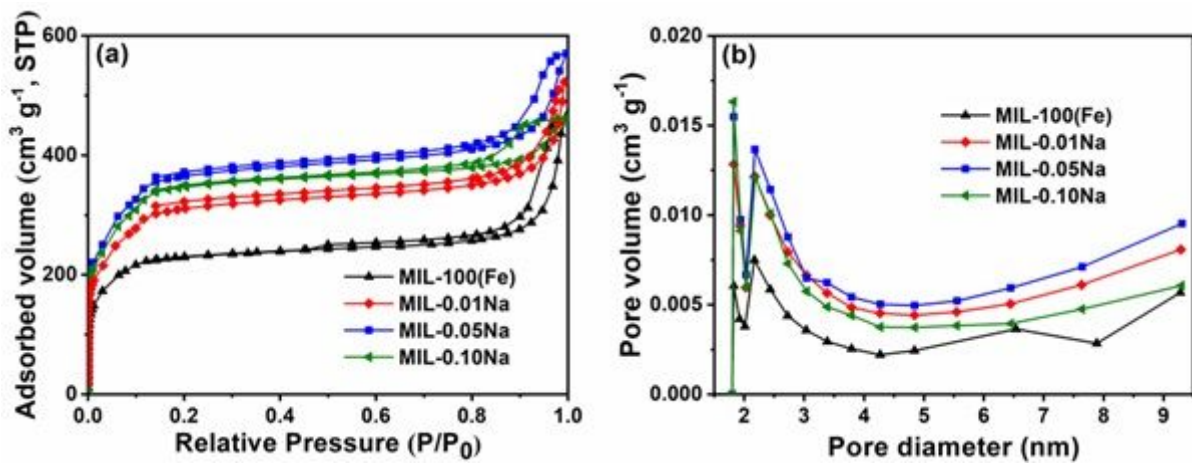


Figure 3

MIL-100(Fe) and MIL-XNa (a) N₂ adsorption-desorption isotherms and (b) pore size distribution

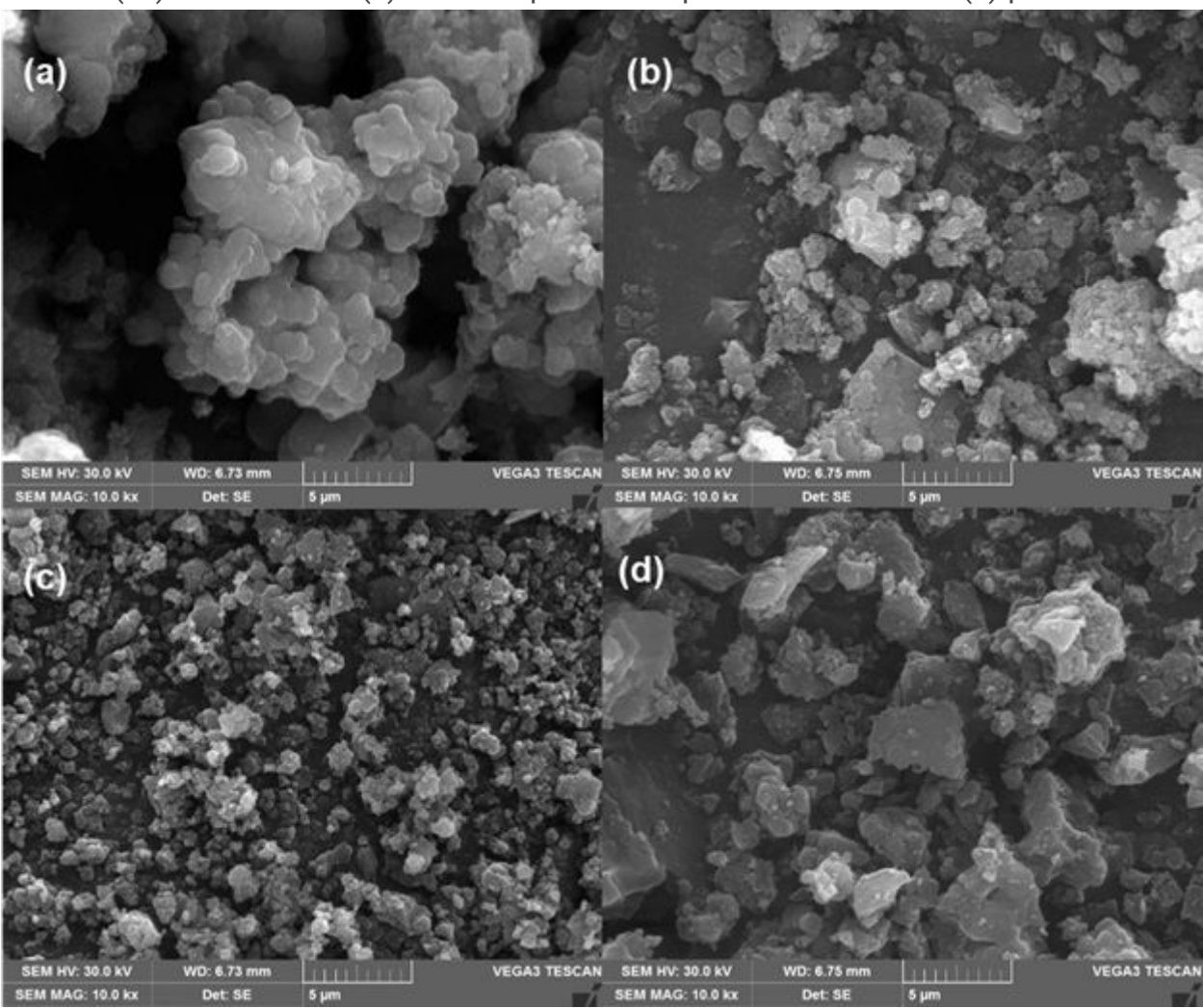


Figure 4

SEM of (a) MIL-100(Fe) (b) MIL-0.01Na (c) MIL-0.05Na and (d) MIL-0.10Na

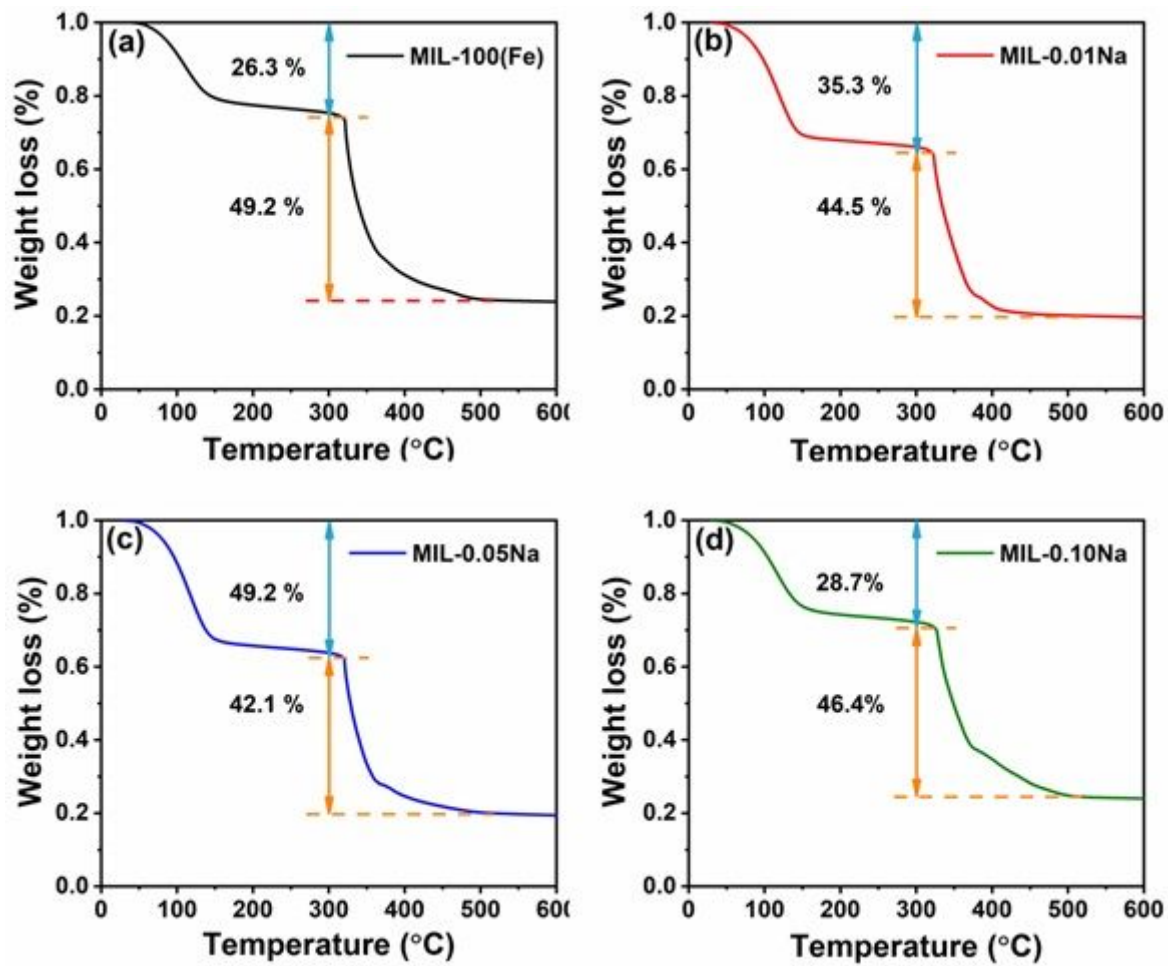


Figure 5

TGA of (a) MIL-100(Fe) (b) MIL-0.01Na (c) MIL-0.05Na and (d) MIL-0.10Na

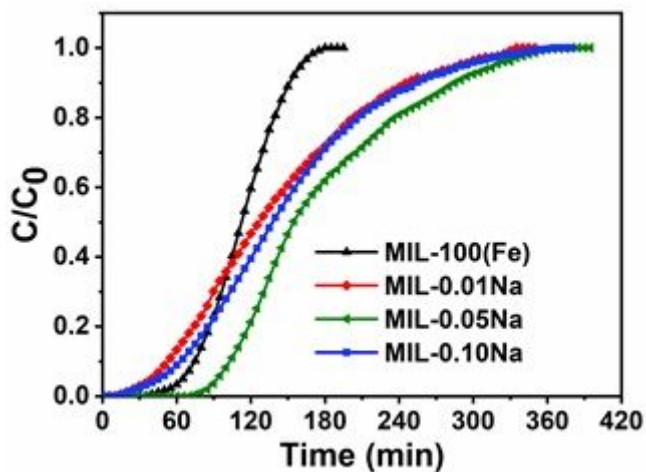


Figure 6

Breakthrough curves with MIL-100(Fe) and MIL-XNa at 400 ppm and 298 K

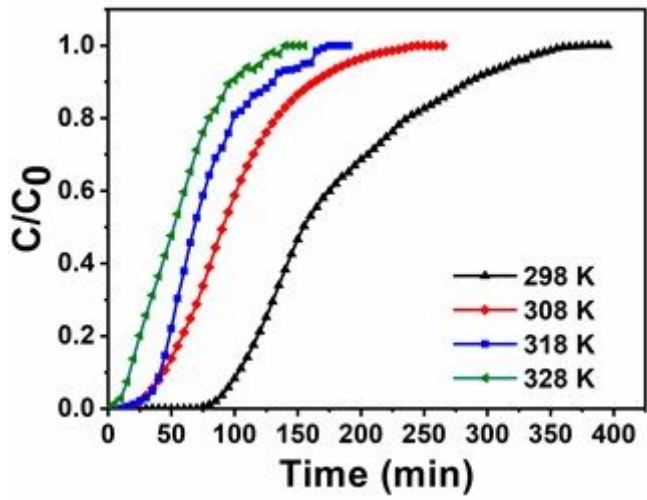


Figure 7

Breakthrough curves with MIL-0.05Na at different temperature

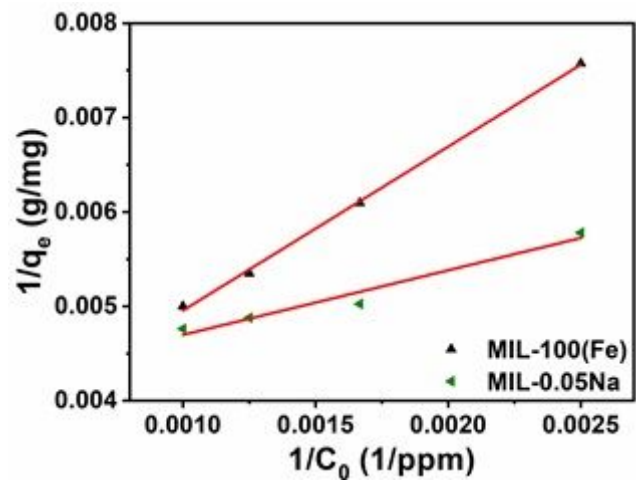


Figure 8

Adsorption isotherms: Langmuir model

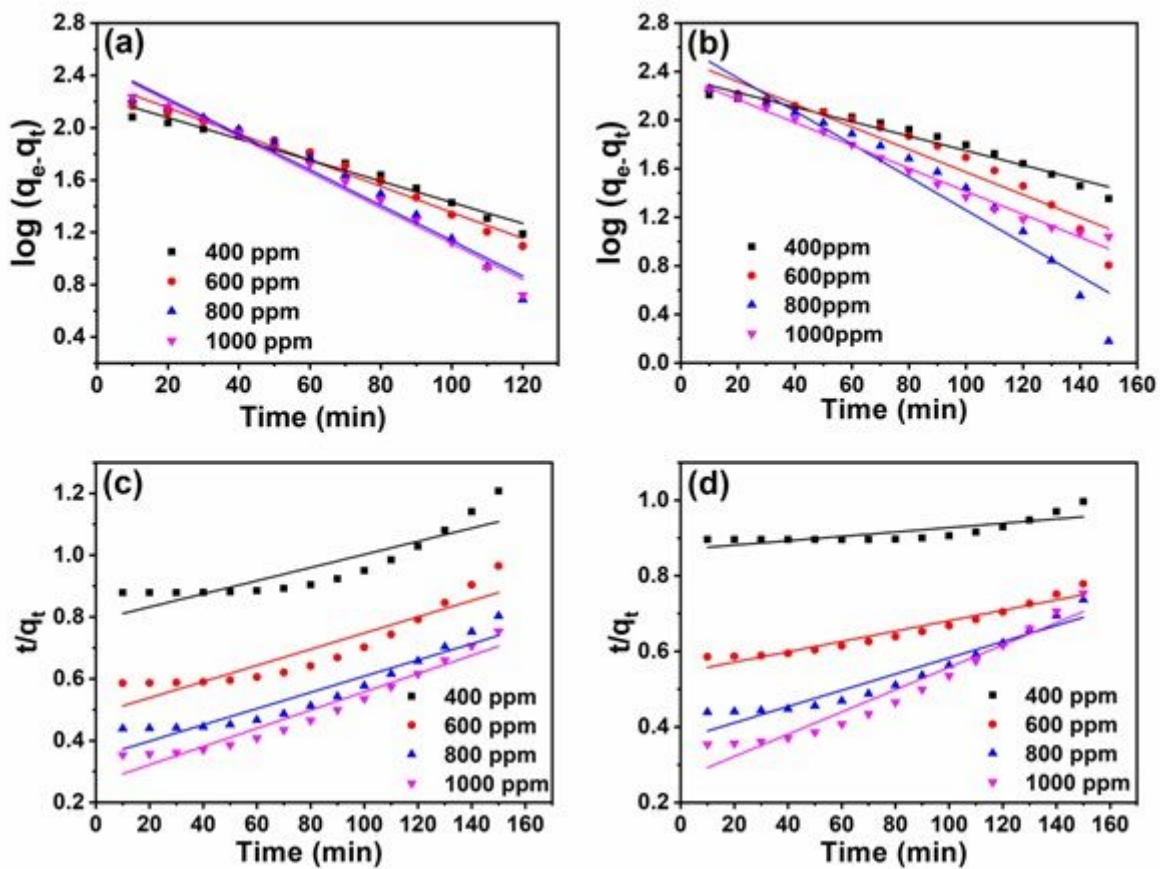


Figure 9

Kinetic fitting of (a) MIL-100(Fe) PFO model (b) MIL-100(Fe) PSO model (c) MIL-0.05Na PFO model and (d) MIL-0.05Na PSO model

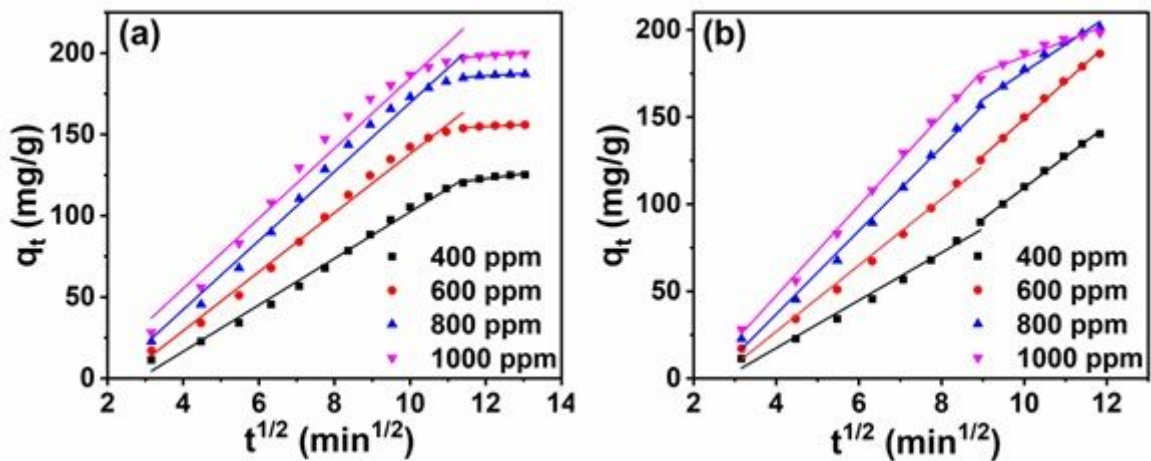


Figure 10

Kinetics of acetone adsorption with (a) MIL-100(Fe) and (b) MIL-0.05Na according to the intra-particle diffusion model

Supplementary Files

This is a list of supplementary files associated with this preprint. Click to download.

- [Scheme1.jpg](#)
- [SupplementaryMaterial.docx](#)